



THE UNIVERSITY *of* EDINBURGH

Edinburgh Research Explorer

Control mechanisms of pore-pressure dissipation in debris flows

Citation for published version:

Zheng, H, Shi, Z, Kaitna, R, Zhao, F, de Haas, T & Hanley, KJ 2023, 'Control mechanisms of pore-pressure dissipation in debris flows', *Engineering Geology*, vol. 317, 107076.
<https://doi.org/10.1016/j.enggeo.2023.107076>

Digital Object Identifier (DOI):

[10.1016/j.enggeo.2023.107076](https://doi.org/10.1016/j.enggeo.2023.107076)

Link:

[Link to publication record in Edinburgh Research Explorer](#)

Document Version:

Peer reviewed version

Published In:

Engineering Geology

General rights

Copyright for the publications made accessible via the Edinburgh Research Explorer is retained by the author(s) and / or other copyright owners and it is a condition of accessing these publications that users recognise and abide by the legal requirements associated with these rights.

Take down policy

The University of Edinburgh has made every reasonable effort to ensure that Edinburgh Research Explorer content complies with UK legislation. If you believe that the public display of this file breaches copyright please contact openaccess@ed.ac.uk providing details, and we will remove access to the work immediately and investigate your claim.



Control mechanisms of pore-pressure dissipation in debris flows

Hongchao Zheng¹, Zhenming Shi¹, Roland Kaitna², Fei Zhao¹, Tjalling de Haas³, Kevin J Hanley⁴

¹Department of Geotechnical Engineering, College of Civil Engineering, Tongji University, China

²Institute of Mountain Risk Engineering, University of Natural Resources and Life Sciences, Vienna, Austria

³Department of Physical Geography, Utrecht University, The Netherlands

⁴School of Engineering, Institute for Infrastructure and Environment, The University of Edinburgh, United Kingdom

Abstract

Debris flows are typically saturated mixtures of debris grains and interstitial slurry consisting of water and clay. Pore pressure in slurry plays a crucial role in the characteristic behavior and runout of debris flows. However, the mechanisms that cause pore pressures to diffuse are still uncertain. Here we report consolidation tests to investigate the effects of debris composition (uniformly graded and widely graded) and slurry density on the dissipation of pore pressure. Pore pressures of debris flows were found to dissipate at contrasting rates ranging from a few seconds to dozens of hours and dissipation time strongly depended on slurry density. We observed an abrupt change in pore-pressure dissipation time at a critical slurry density. We propose that a critical pore throat controls the permeability of a debris material and regulates the pore-pressure dissipation based on percolation theory. This hypothesis is verified by pore-network models from a micro-computed tomography analysis with high resolution. The critical pore throat of the uniformly graded debris material is larger than that of widely graded debris material due to the difference in the porosity. The permeabilities and hydraulic diffusivities of debris flows significantly decrease once critical pore throats are blocked, resulting in a change of pore-pressure dissipation. Critical slurry density is approximately linearly correlated with the porosity of debris flows. Our results highlight opportunities to use micro-structural properties for interpreting debris-flow behavior.

Keywords: debris flows, pore pressure, dissipation rate, slurry density, hydraulic diffusivity

1. Introduction

Debris flows are gravity-driven, multiphase flows of which the solid fraction is coarse debris and the fluid fraction, termed slurry, is water containing clay particles in solution and suspension (e.g., Iverson, 1997; Takahashi, 2007; Pudasaini, 2012; Zheng et al., 2021a). Debris flows are ubiquitous hazards in mountain areas, due in part to the difficulty in predicting their transportation and deposition processes (Wang et al., 2003; Guthrie et al., 2010; Chen and Wu, 2018; Hu et al., 2021; Zheng et al., 2021b). These processes, which depend on particle-scale mechanics, are affected by the debris composition, segregation and the persistence of non-hydrostatic pore pressure (Iverson, 1997; Kaitna et al., 2014; de Haas et al., 2015; Zheng et al., 2018, 2022).

Pore pressure strongly regulates the mobility and deposition of debris flows as frictional resistance of granular material scales with normal stress (Jop et al., 2006). The effect can be conceptualized by Terzaghi's effective stress principle (Terzaghi, 1943) that pore pressure in excess of hydrostatic pressure can mediate effective stress, reduce shear resistance and thereby enhance debris-flow mobility (Pierson, 1981; Iverson, 1997). Debris flows have negligible to high interstitial pore pressures and thus can be liquefied at different liquefaction ratios and durations depending on the diffusion timescale (McArdell et al., 2007; McCoy et al., 2010; Nagl et al., 2020). Affected by the magnitude of excess pore pressure, some debris flows come to rest after only a short transport distance, freezing on steep channel reaches in their watershed or at the fan apex, while other debris flows traverse the entire length of the fan, eventually spreading out as thin, tabular deposits on gentle slopes of the fan margin (Bardou et al., 2003; Tiranti et al., 2008; McCoy et al., 2010; Hürlimann et al., 2015). These contrasting scenarios may even occur in the same torrents (Suwa et al., 2009). Therefore, it is of vital importance to interpret the dissipation of pore pressures to precisely delineate and predict the areas endangered by debris flows (Scheidl and Rickenmann, 2010; D'Agostino et al., 2010).

Two main processes of propagation and consolidation need to be considered after debris-flow initiation (Tayyebi et al., 2021). The characteristic times of propagation and consolidation are crucial for flow behavior. When the consolidation time is much smaller than propagation time, pore pressures dissipate rapidly and the flow behavior is described as drained. It becomes undrained when the dissipation time is much longer than the propagation time. Pore pressure persists during propagation until the debris flow reaches the deposition area when the time for pore-pressure dissipation has the same magnitude as the propagation time. Therefore, the dissipation timescales of debris flows obtained from consolidation tests are meaningful to explain flow dynamics.

Excess pore-fluid pressure of natural and laboratory debris flows is sustained during flow (McCoy et al., 2010; Kaitna et al., 2016). This is because pore-pressure dissipation is compensated by the generation of pore pressure induced by pore

dilatation, grain collisions, centripetal acceleration, Reynolds stresses and other mechanisms (Iverson and LaHusen, 1989; Hotta and Ohta, 2000). To isolate the effects of pore-pressure generation, the dissipation behavior of pore pressure is usually analyzed for debris flows after the cessation of motion.

Excess pore pressures can persist in debris flows for periods ranging from fractions of seconds to hours (Iverson and LaHusen, 1989; Kaitna et al., 2016). The dissipation of excess pore pressure p_e in depositional consolidation has often been represented by a diffusion model (Major, 2000)

$$\frac{\partial p_e}{\partial t} = D \frac{\partial^2 p_e}{\partial H^2} \quad (1)$$

where H is the height of the deposited debris mixture. The hydraulic diffusivity $D = E_c k_c / \eta$, where E_c is the modulus reflecting the bulk stiffness of the debris material, η is the dynamic viscosity of the pore slurry and k_c is the permeability of the debris flow. Pierson (1981) conducted the first widely known experimental investigation of pore-pressure dissipation and observed that the time for elevated pore-pressure dissipation increased by several orders of magnitude when the slurry density increased slightly as a result of small volumes of dissolved clay and/or silt. Iverson (1997) termed this phenomenon the nonlinear diffusion behavior of pore pressure. Later laboratory measurements of pore pressures in small and large volumes of debris flows after deposition showed similar results (Major, 2000; de Haas et al., 2015; Kaitna et al., 2016). However, the underlying mechanisms that cause this diffusion behavior remain unclear.

Recently, multiple digital image techniques with high resolution have been developed for characterizing geological structure and mineral composition in geotechnical engineering. Common digital image techniques for pore structure in the laboratory include X-ray diffraction, X-ray fluorescence, nuclear magnetic resonance, transmission electron microscopy, atomic force microscopy, X-ray computed tomography scanning (micro-CT), and scanning electron microscopy (Cui et al., 2022). Taylor et al. (2015) have proposed methods to measure pore throats of sand material from micro-CT data. However, the permeability reduction of a porous medium due to pore-throat clogging and the resulting change of pore-pressure dissipation mode have not been investigated.

The pore-pressure diffusion of a debris flow is primarily controlled by debris composition and slurry density (Iverson and George, 2014). For the former, the initial permeability of a porous medium is affected by the debris composition (Iverson and George, 2014); for the latter, the viscosity of the pore slurry significantly increases with increasing slurry density (Major, 2000). Further research is therefore needed to investigate independently the effects of slurry density and debris composition of debris flow on the dissipation process of pore pressure.

To fill the knowledge gaps mentioned above, we propose a hypothesis of permeability reduction of debris flow based on percolation theory. We investigate the effects of debris composition and slurry density on pore-pressure dissipation by a

series of consolidation tests. We use micro-CT analysis to quantify the spatial distribution of pore networks and permeability of the tested debris materials to interpret pore-pressure dissipation in consolidation tests. We identify the existence of critical pore throats and show that clogging of these pore throats results in a rapid reduction in the permeability and diffusivity of debris flow.

2. Hypothesis

Void spaces in a porous medium of debris flow can be represented as a pore network composed of pores and pore throats (Sharma and Yortsos, 1987). Adjacent pores are connected by pore throats (Fig. 1B). Pore pressure in interstitial slurry is dissipated through the pore network.

Driven by excess pore pressures, suspended fines migrate with the pore fluid and block pore throats to cause a reduction in the permeability (Fig. 1C). Hydraulic diffusivity of pore pressure is therefore reduced with the permeability. At a critical proportion of blocked pore throats, the pore network breaks into unconnected clusters, resulting in a significant decrease in the overall permeability and hydraulic diffusivity. We hypothesize the existence of a critical pore throat that controls the permeability of a porous medium of debris flow based on percolation theory (Kirkpatrick, 1973). The critical pore throat is defined as the obstructed pore throat when the pore network separates into isolated pore clusters (Fig. 1D).

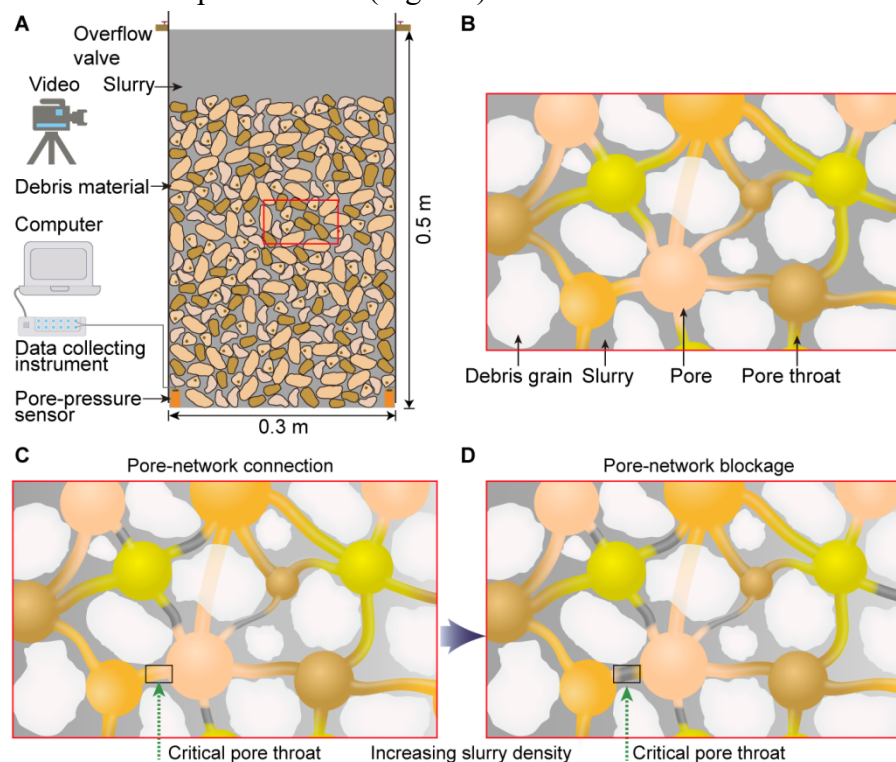


Fig. 1. A: Sketch of the setup for the consolidation tests. B: Concept of the pore network in a porous medium; pores are connected to each other by pore throats. Voids between debris grains are filled with the grey slurry. Pores and pore throats are denoted by colorful balls and pipelines. C: Pore-network connection from the left to the right through interlinked pore throats (without grey segments). Pore throats with

grey segments are clogged by slurry fines. D: Pore-network blockage when the critical pore throats are obstructed. Pores on the left cannot be connected with pores on the right through the pore throats.

3. Methods and materials

3.1 Consolidation tests

To investigate the process of pore-pressure dissipation, we conducted self-weight consolidation tests under closely controlled conditions (Fig. 1A). In each consolidation test, we rapidly poured a mixture of debris grains and slurry with a volume of 35.3 liters into a transparent cylindrical tank, allowing the consolidation process to be observed. The mixture height in the tank was 0.5 m after pouring. A scale on the surface of the tank was used to discern the height of deposited debris H . The bottom of the tank was sealed to achieve an impermeable boundary; the tank was free to drain from the top through two symmetrically arranged overflow valves.

Table 1 Compositions of the tested mixtures

Case	GSD	C_d	ρ_s (kg/m ³)
U1	U	0.2	1000
U2	U	0.4	1000
W1	W	0.2	1000
W2	W	0.4	1000
U3	U	0.2	1206
U4	U	0.4	1240
U5	U	0.4	1275
W3	W	0.2	1206
W4	W	0.4	1240
W5	W	0.4	1275
U6	U	0.2	1297
U7	U	0.4	1385
W6	W	0.4	1385

Note: GSD denotes grain size distribution as shown in Table 2, U and W denote uniformly graded and widely graded debris materials, respectively. ρ_s = slurry density, C_d = volumetric concentration of debris grains, $C_d = V_d / V_m$, where V_d is debris-grain volume and V_m is the mixture volume.

We systematically varied the debris type and volumetric concentrations of debris grains and slurry to differentiate the effects of debris composition and slurry density on the dissipation of pore pressure (Table 1). We prepared two types of debris materials containing size fractions of quartz particles between 0.5–2.0 mm (uniformly graded) and 0.5–5.0 mm (widely graded), as shown in Table 2. Debris concentrations were 0.2 and 0.4, and slurry densities were within the range of 1000–1385 kg/m³. Slurry consisted of a mixture of water and kaolin which is the main component of

debris-flow clay. 78.3% of the fines of the kaolin by volume had a grain size less than 2 μm , and 99.8% less than 45 μm .

Table 2 Grain size distributions of debris material

Debris type	Grain size (mm)	Percentage	w	k_s (10^{-11} m^2)	E_c (10^6 Pa)
Uniformly graded	0.5 – 1.0	40%	1.9	7.5	1.2
	1.0 – 2.0	60%			
Widely graded	0.5 – 1.0	25%	3.0	4.0	1.5
	1.0 – 2.0	37.5%			
	2.0 – 5.0	37.5%			

Note: sorting coefficient $w = d_{75}/d_{25}$, k_s and E_c are the permeability and compression modulus of a debris grain, respectively.

A concentric cylinder viscosimeter (Anton Paar, MCR 301) was used to obtain the rheology of slurries. The shear rate was determined to be $0.1\text{--}1 \text{ s}^{-1}$ considering the low seepage velocity of pore slurry during consolidation. The temperature was $20 \text{ }^\circ\text{C}$. As shown in Fig. 2, the dynamic viscosity of the slurry containing kaolin clay was significantly higher than that of pure water. The permeabilities k_s of uniformly and widely graded debris with the same dry densities as the consolidation tests were measured from constant-head permeameter tests. k_s of uniformly graded debris was larger than the value for widely graded debris (Table 2). The compression modulus E_c was measured from axial strain in a $20 \text{ cm} \times 20 \text{ cm} \times 20 \text{ cm}$ cell under 50 kPa confinement.

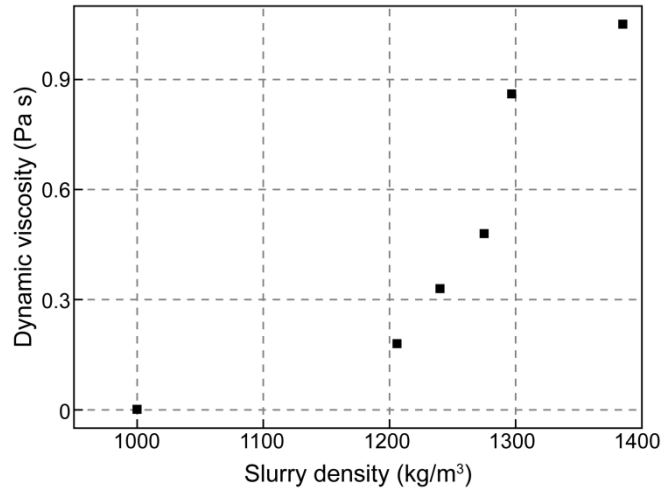


Fig. 2. Dynamic viscosity versus slurry density

The transient behavior of each debris mixture during consolidation was captured by a video recording at a frame rate of 25 Hz. The attendant pore pressure at the bottom of the tank was measured with two electronic pressure sensors with a precision of 20 Pa. Two pressure sensors distanced by 30 cm were mounted symmetrically on the bottom of the tank. Both pressure sensors had been fully saturated by evacuation before pouring. Data from each sensor were digitally logged at 20 Hz for the test duration. The test procedure is listed as follows:

(1) The mixture of debris and slurry was constantly blended in a 70 liter bucket using a portable rotary mixer for nearly 20 minutes.

(2) The mixture was rapidly poured from the bucket into the tank with an inner diameter of 0.3 m and a height of 0.6 m. The resulting mixture height in the tank was 0.5 m (Fig. 1A).

(3) The pore-fluid pressure at the bottom of the tank was measured and the transient behavior of the debris mixture was recorded.

(4) The measurement terminated when the measured pore pressure declined to hydrostatic pressure.

The pore-pressure dissipation time t_d was measured from the end of debris pouring until when the pore pressure declined to hydrostatic pressure. The transient excess pore pressure for a no-flux basal boundary condition is given by (Major, 2000)

$$p_e(H, t) = 8p_{e0} \sum_{n=0}^{\infty} \frac{1}{(2n+1)^2 \pi^2} \cos(\lambda_n H) e^{-\lambda_n^2 D t} \quad (2)$$

where p_{e0} represents the initial excess pore pressure at the bottom of the tank. Herein the eigenvalues are defined as $\lambda_n = \frac{(2n+1)\pi}{2H}$. The hydraulic diffusivity D and permeability k_c of debris flow were calculated from t_d and p_{e0} .

3.2 Micro-CT tests

Micro CT facilitates three-dimensional (3D) imaging of samples in a non-destructive way. A schematic diagram of our synchrotron-based micro-CT setup is given in Fig. 3. A micro-CT analysis was carried out to derive information on the micro-structure and the pore network of the tested debris materials.

The sample length is more than five times the size of the largest grain as a compromise between the field of view and scanning resolution. The inner diameter and height of the cylindrical sample for scanning were 30 mm. The scanning resolution was determined to be $30 \times 30 \times 30 \mu\text{m}$ per voxel (Xradia 520 Versa). The cylindrical sample box was made of polymethyl methacrylate (Fig. 3B). This was distinguished easily from debris grains and void air because of a significant density difference. Debris materials were filled into the sample box in 3–5 stages and evenly compacted by slightly tapping with a plastic rod. The dry densities of debris material used in the micro-CT scans were consistent with those of uniformly graded ($1428.2 \pm 19.9 \text{ kg/m}^3$) and widely graded debris ($1605.5 \pm 24.1 \text{ kg/m}^3$) in the consolidation tests.

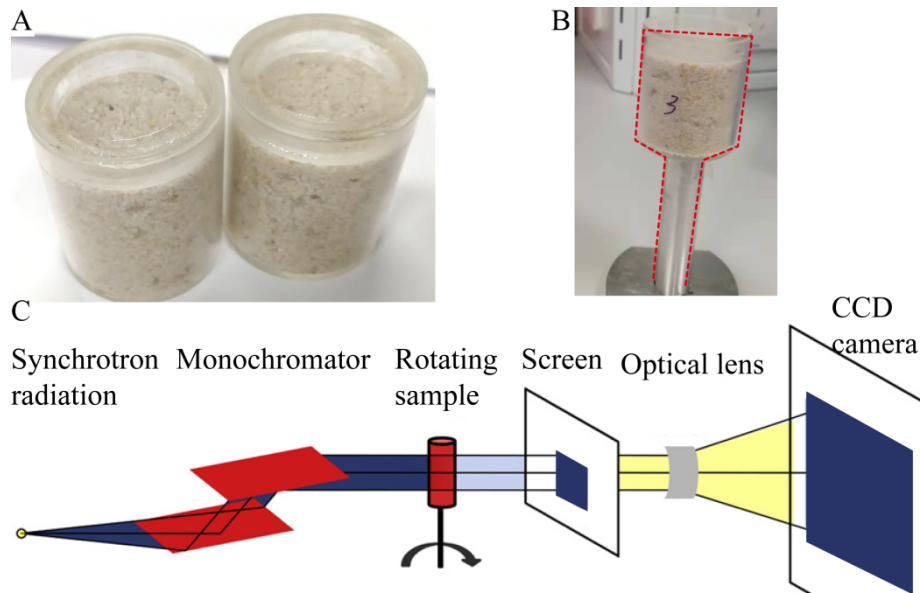


Fig. 3. Experimental setup for scanning uniformly graded and widely graded debris. A: samples of debris grains; B: rotating sample in micro-CT scanner; C schematic diagram of synchrotron-based micro-CT setup.

A 3D CT model was firstly constructed based on layered 2D slices (Fig. 4). A nonlocal means filter was applied to eliminate noise and smooth the images while preserving the edges and details (Fig. 4C). The pore phase of debris material was extracted based on the grayscale differences between the pores and debris grains. Then, the pore phase was subdivided into separate pore bodies (Fig. 4D). Pores and the surrounding connected pores for each were determined. It should be noted that closed pores have no effect on the processes of seepage and consolidation, and thus they were not considered. Pore throats were defined as the boundaries between connected pores using the watershed segmentation method (Taylor et al., 2015). Finally, a 3D pore-network model was quantitatively established, as shown in Fig. 4F. The model processing was performed with Avizo (VSG Inc., Burlington, MA, USA).

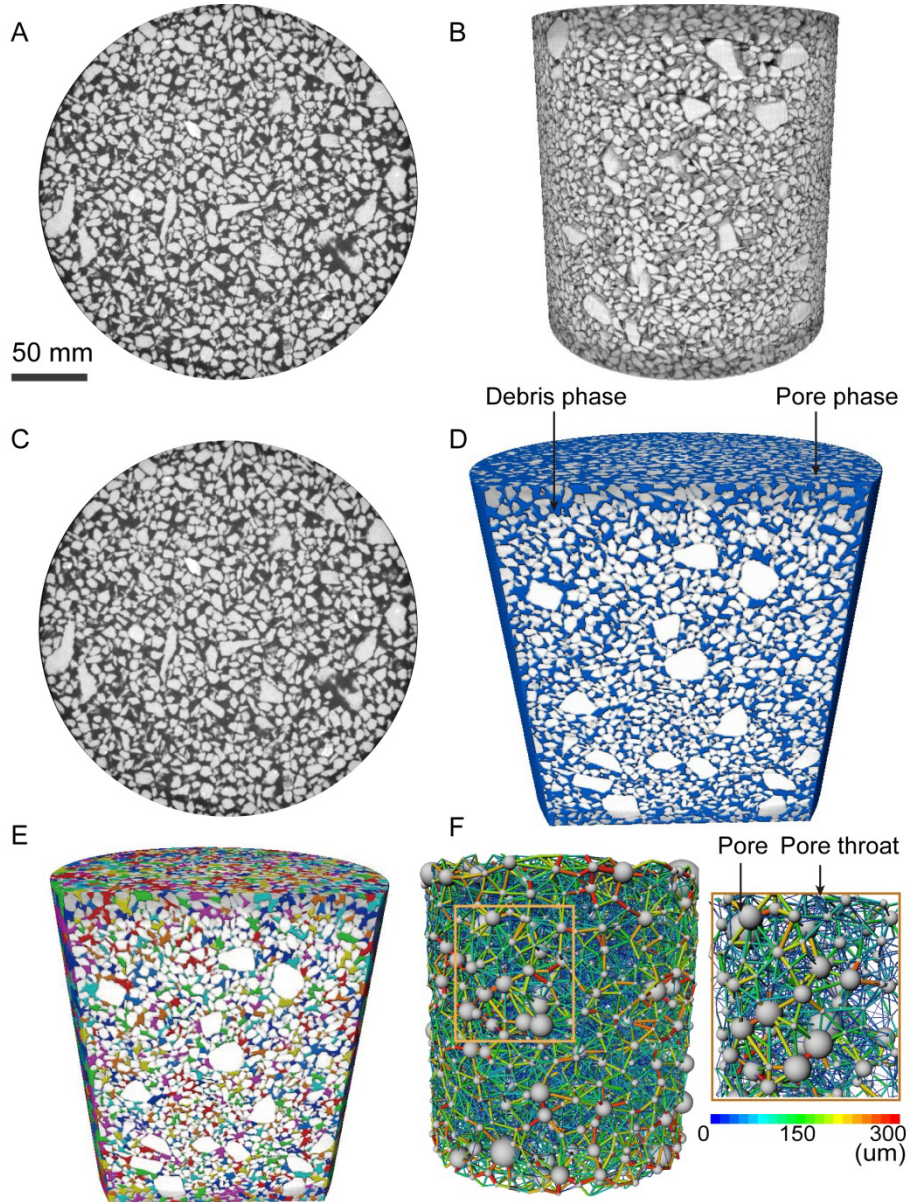


Fig. 4. Establishment of pore-network model. A: a greyscale raw cross-sectional 2D slice. B: 3D alignment of 2D slices. C: denoised cross-sectional 2D slice by nonlocal means filter. D: pore-phase extraction. E: pore-phase segmentation by micro-CT analysis. White represents the debris phase and various colors distinguish adjacent pore spaces. F: pore-network model. The rightmost figure is an enlargement of the region within the orange border.

The connections between the pores and pore throats were recorded and physical parameters like pore location, pore number N_p , coordination number N_c (the number of pore throats emanating from a pore), pore-throat radius r and characteristic length l of each pore throat were calculated. The spatial distribution of a 3D pore network was obtained. The size of the critical pore throat of the pore network r_c was obtained by progressively blocking pore throats of increasing size in steps equal to the scan resolution ($30 \mu\text{m}$) until the pore-network connectivity was broken.

The permeability of a pore network is calculated as follows. For steady-state flow of an incompressible fluid, mass conservation for each pore body is described by

$$\sum_{i \rightarrow j}^{N_c} q_{ij} = 0 \quad (3)$$

where the summation is performed for all pores j connected to the pore i and q_{ij} represents the flow rate between pore i and pore j . The relation between q_{ij} and pressure drop ($p_i - p_j$) for a Darcy's flow is

$$q_{ij} = g_{ij} (p_i - p_j) \quad (4)$$

where g_{ij} represents the hydraulic conductivity of the throat between pore i and pore j . g_{ij} of a cylindrical throat is given by Poiseuille's law:

$$g_{ij} = \frac{\pi r_{ij}^4}{8\eta l_{ij}} \quad (5)$$

A linear matrix equation is obtained from Eqs. (3) and (4):

$$G^* P = S \quad (6)$$

where G is the conductance matrix of dimension $N_p \times N_p$ and S represents the pressure boundaries applied at the inlet and the outlet of the pore network. The permeability k_m of the pore network is deduced from

$$k_m = \frac{Q}{\Delta P} \frac{\eta L}{A} \quad (7)$$

where the total flow rate Q is obtained for each pair of pores i, j intersecting an arbitrary cross section of a surface A . ΔP and L are the pressure gradient between the inlet and the outlet of the pore network and its length, respectively. k_m calculated from Eq. (7) is independent of the applied pressure gradient ΔP and dynamic viscosity η of the pore slurry. k_m is related to the pore-network structure.

The permeabilities k_{m0} calculated from the pore-network modeling were $7.1 \times 10^{-11} \text{ m}^2$ and $3.9 \times 10^{-11} \text{ m}^2$ for uniformly graded and widely graded debris materials, respectively. These values of k_{m0} matched the permeabilities k_s obtained from constant-head permeameter tests (Table 2), confirming the accuracy of the pore-network model.

4. Results and analysis

4.1. Experimental results of consolidation

Pore pressures of the experimental debris flow mixtures exhibited sharply contrasting dissipation modes as the slurry density ρ_s increased. For the four water-saturated debris mixtures with $\rho_s = 1000 \text{ kg/m}^3$ (uniformly graded mixtures U1–U2 and widely graded mixtures W1–W2), pore pressures rose abruptly during pouring and then dissipated rapidly within a few seconds (Fig. 5A). For debris mixtures with $\rho_s = 1206\text{--}1275 \text{ kg/m}^3$ (U3–U5 and W3–W4), pore pressures transitioned from slow to fast dissipation (Fig. 5B). The duration of slow dissipation was approximately 2–7 minutes and the total dissipation time was around 6–32 minutes. For debris mixtures

with $\rho_s = 1275\text{--}1385 \text{ kg/m}^3$ (U6–U7 and W5–W6), pore pressure dissipated slowly and lasted for more than 16 hours (Fig. 5C).

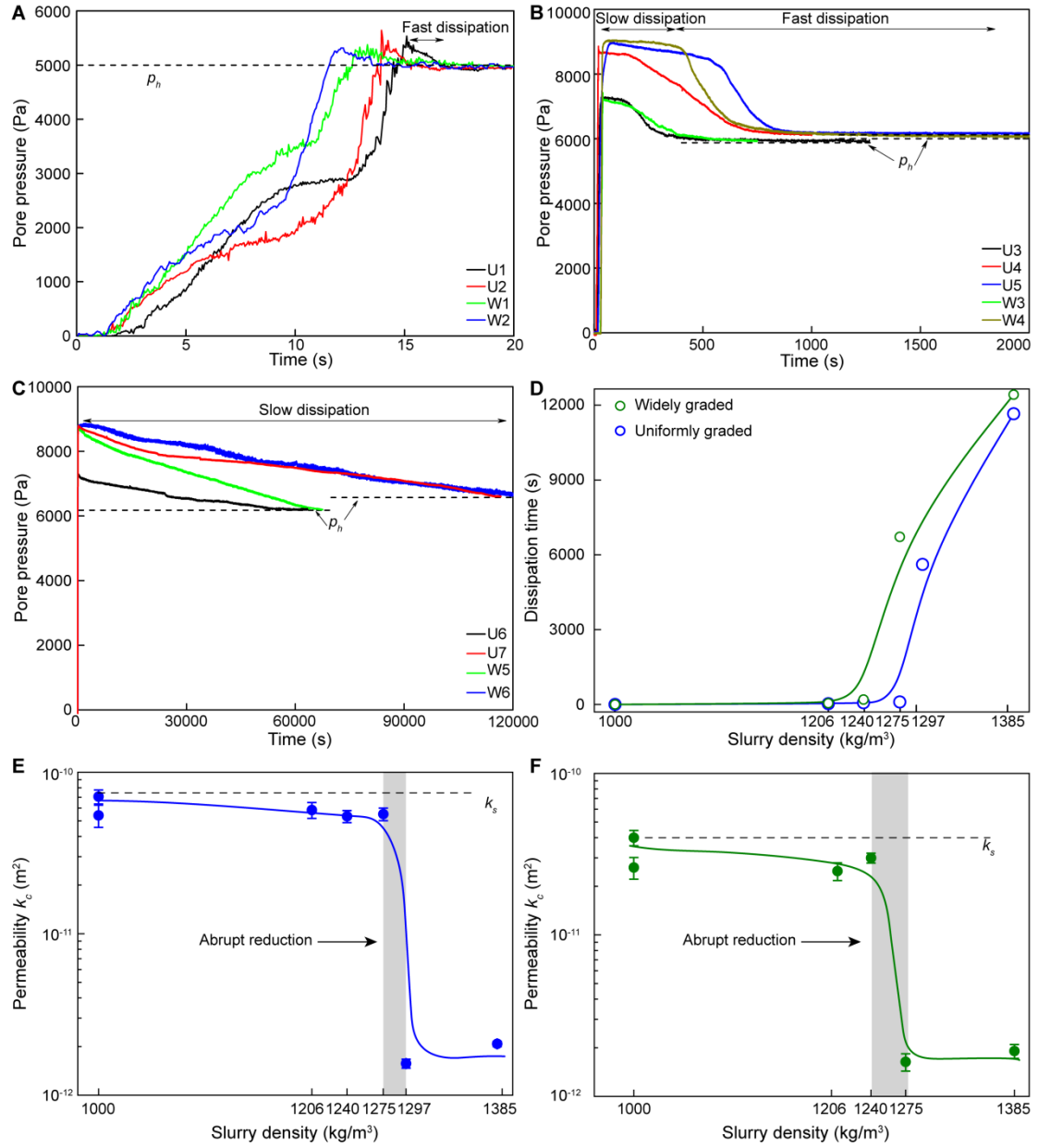


Fig. 5. Pore pressures measured in consolidation tests. A: Fast dissipation of pore pressure for U1–U2 and W1–W2. The dashed lines denote the hydrostatic pressure p_h . B: Slow to fast dissipation for U3–U5 and W3–W4. C: Slow dissipation for U6–U7 and W5–W6. D: Relation between pore-pressure dissipation time t_d and slurry density. E: Permeability reduction of uniformly graded debris flow. The error bars for k_c are propagated from the errors in H and t_d . F: Permeability reduction of widely graded debris flow. The permeabilities k_s measured from constant-head permeameter tests were approximately equal to k_c for U2 and W2.

There are two thought-provoking observations. One is that pore-pressure dissipation time t_d increased by approximately two orders of magnitude due to an increase in ρ_s of less than 3%: compare W4 and W5, or U5 and U6 (Fig. 5D). Values

of t_d were nearly tens of minutes for W4 and U5. By contrast, dozens of hours were needed to dissipate pore pressure for W5 and U6. This is in accordance with data of laboratory experiments reported in the literature (Pierson 1981; Major, 2000; de Haas et al., 2015; Kaitna et al., 2016). For uniformly graded debris, a critical slurry density ρ_{sc} of 1275–1297 kg/m³ caused an abrupt change in t_d , which was larger than ρ_{sc} (1240–1275 kg/m³) of widely graded debris. t_d transitioned to increase slowly after the abrupt change by comparing W5 and W6 as well as U6 and U7. The second observation is that the pore pressures for U3–U5 and W3–W4 displayed a slow-to-fast dissipation mode (Fig. 5B), seemingly in conflict with diffusion Eq. (2) that predicts a gradual decrease of the pore-pressure dissipation rate as observed for other scenarios.

The hydraulic diffusivity D had a magnitude of 10^{-2} m²/s for water-saturated debris mixtures, decreasing to a magnitude of 10^{-4} m²/s for U3–U5 and W3–W4 (Table 3). The reduction in D is mainly attributed to the increase of dynamic viscosity η . The back-calculated permeability k_c from Eq. (2) for U3–U4 and W3 decreased by ~20% compared to water-saturated debris mixtures, and remained on the order of 10^{-11} m² (Figs. 5E and 5F). D decreased to a magnitude of 10^{-6} m²/s for U6–U7 and W5–W6. Here η increased less than threefold compared to U5 and W4, respectively, while k_c significantly decreased to the order of 10^{-12} m². The pore pressures of the debris flow mixtures thus show a different diffusion behavior which was caused by the permeability reduction with respect to slurry density.

Table 3 Consolidation coefficients of debris mixtures

Case	t_d (s)	p_{e0} (Pa)	p_h (Pa)	D (m ² /s)	η (Pa s)	k_c (10^{-11} m ²)
U1	1.1	467	4905	0.06479852	0.001	5.40
U2	2.75	448	4905	0.0847046	0.001	7.06
W1	1.4	364	4905	0.0391916	0.001	2.64
W2	3.5	314	4905	0.0599690	0.001	4.00
U3	305	1327	5915	0.0003885	0.18	5.83
U4	700	2506	6082	0.0001938	0.33	5.33
U5	998	2652	6254	0.0001376	0.48	5.50
W3	496	1206	5915	0.0002065	0.18	2.50
W4	1960	2200	6082	0.0001361	0.33	2.99
W5	67200	2735	6254	0.0000051	0.48	0.16
U6	56140	1095	6362	0.0000020	0.86	0.15
U7	116546	2210	6793	0.0000027	1.05	0.24
W6	124215	2289	6793	0.0000027	1.05	0.19

Note: t_d denotes dissipation time and p_{e0} denotes initial excess pore pressure during consolidation. p_h is considered as isotropic stress emerging from weight of the fluid and the fine particles (kaolin) held in suspension.

A comparison of recorded snapshots shows that the consolidation processes of debris flows with a low slurry density (W3–W4 and U3–U5) are distinct from those of

W5–W6 and U6–U7 with a high slurry density. Taking W3 and W5 as an example, debris grains in W3 were masked by surrounding slurry just after pouring and it was difficult to discern the sediment distribution (Fig. 6). Debris grains gradually emerged as interstitial slurry was continuously squeezed out. Finally, a visible boundary appeared between the deposited debris grains and the slurry above at the end of pore-pressure dissipation. By contrast, the mixture of debris and slurry in W5 seemed to be uniformly distributed throughout the tank. The water slowly escaped from the top of the debris mixture. There was no perceptible change from the initiation of pore-pressure dissipation to the end, indicating that interstitial slurry was trapped in the intergranular pores of debris grains. These different consolidation processes were also observed by comparing U3–U5 with U6–U7.

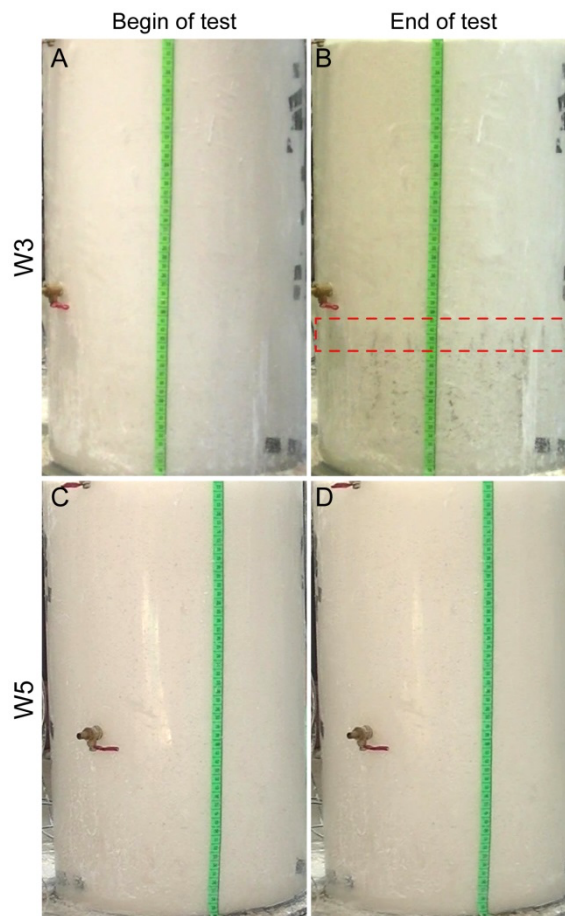


Fig. 6. Comparisons of consolidation processes in W3 and W5. A, B: Snapshots at the initiation and end of pore-pressure dissipation, respectively, in W3. Debris grains gradually emerged as interstitial slurry was continuously squeezed out. This process was also similar in W4 and U3–U5. C, D: Snapshots at the initiation and end of pore-pressure dissipation, respectively, in W5. This process was also similar in W6 and U6–U7. The dashed box on Fig. 6B denotes the boundary position between deposited debris and the slurry above. No boundary developed in W5 from the initiation of pore-pressure dissipation to the end.

4.2. Micro-CT analysis

The coordination numbers of pores (the number of pore throats emanating from a pore) vary from 1 to 25 for both debris materials, indicating that the pore-network structure is complex. The radii r of most pore throats are distributed within the range of 0–300 μm . The number of pore throats in the uniformly graded material is larger than that of the widely graded material (Figs. 7A and 7B). The pore-throat sizes of both debris materials are well represented by a truncated Gaussian distribution as

$$N = \frac{a}{\sqrt{2\pi}\sigma} \exp\left(-\frac{(r-r_m)^2}{2\sigma^2}\right) \quad (8)$$

where a is a coefficient. The pore throats in the uniformly graded material had the same mean value r_m (96 μm) and variance σ^2 (52 μm) as those in the widely graded material.

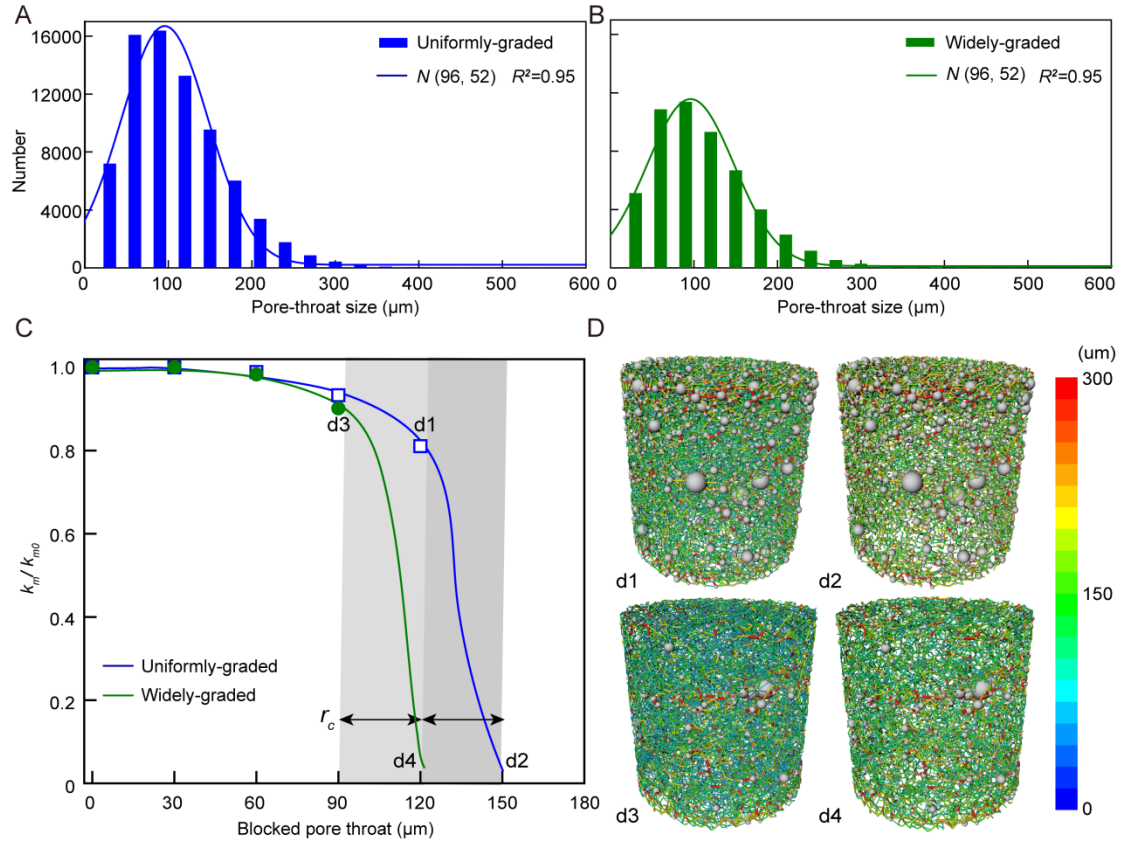


Fig. 7. Pore-throat distribution and permeability reduction as pore throats are progressively blocked. A: Pore-throat sizes in uniformly graded debris material. R^2 is the coefficient of determination. B: Pore-throat sizes in widely graded debris material. C: Permeability reduction in uniformly graded and widely graded material from the pore-network modeling in Eq. (7). k_{m0} denotes the permeability without pore throat blockage. D: Critical pore throat determined by blocking connected pore throats. Pore throats are larger than 120 μm (d1) and 150 μm (d2) in uniformly graded debris and 90 μm (d3) and 120 μm (d4) in widely graded material (Figure C). It is assumed that closed pores have no effect on the processes of seepage and consolidation and thus they were not considered in this calculation.

The permeability k_m of the pore network decreased as pore throats were progressively blocked, as shown in Fig. 7C. The increment of blocked pore throats was the scan resolution. The calculated permeability was reduced by nearly 20% when blocked pore throats were smaller than the critical pore-throat size r_c . Pore-network connectivity was lost once the critical pore throats were blocked and the overall permeability significantly decreased. The reduction processes of the permeability observed from the pore-network modeling are consistent with the consolidation tests by comparing Fig. 7C and Figs. 5E and 5F. This suggests that the permeability of a debris-flow mixture in consolidation tests is reduced by pore-throat blockage. These results show that seepage through pore throats smaller than r_c was minor and the breakage of a connected pore network occurred when the critical pore throats were blocked. The sizes of critical pore throats r_c of uniformly graded and widely graded materials were in the range of 120–150 μm and 90–120 μm , respectively.

Micro-CT analysis implies that the permeability of debris-flow mixtures is regulated by the critical pore throats. On this basis we attempt to interpret the shape of measured pore-pressure dissipation curves which showed three different modes: fast, a transition from slow to fast, and slow (Figs. 5A–5C). For U1–U5 and W1–W4, the pore network stayed connected and a high permeability of debris flow was preserved, allowing pore pressure to dissipate through channels having an approximate size of r_c ($\sim 120 \mu\text{m}$) which resulted in a high diffusivity (10^{-4} – $10^{-2} \text{ m}^2/\text{s}$). In contrast, when all pore throats less than or equal to r_c were blocked, the pore network was disconnected and the fines in slurry were trapped among the intergranular pores as observed in U6–U7 and W5–W6 (Fig. 6). A low permeability (10^{-12} m^2) was generated and the pore pressure slowly dissipated through pore channels smaller than r_c , which led to a diffusivity on the order of $10^{-6} \text{ m}^2/\text{s}$. For U3–U5 and W3–W4, fines in slurry were not sufficient to block all available pore throats less than or equal to r_c and the slurry was expelled through the open pore throats driven by the excess pore pressure, indicated by Figs. 6A and 6B. At the beginning of consolidation, the attendant pore pressure slowly dissipated during initial migration of fines because pore throats were temporarily filled with suspended fines, resulting in a low permeability (Fig. 5B). Thereafter, pore-network connectivity gradually enhanced and the permeability of debris flow was restored due to squeezing out of a portion of suspended fines. Preferential flow paths through large pore throats were developed, contributing to the rapid dissipation of pore pressure.

5. Discussion

In this section, the relations between critical pore throats and the slurry density of debris flows are first analyzed. Then, the effect of slurry density on the permeability and effect of pore pressure on debris-flow behavior are discussed. Finally, implications for natural debris flows inferred from our experiments and limitations are presented.

5.1 Critical pore throat and slurry density

The critical slurry density ρ_{sc} is approximately linearly correlated with the porosity n of the tested debris flows and related data from literature (Fig. 8). This porosity within the range of 0.3–0.5 is consistent with those of natural debris flows (Iverson, 1997). The number of pore throats (especially large pore throats) increases with increasing n (Sharma and Yortsos, 1987). The size of the critical pore throat thus increases with porosity, explaining the increase in the number of fines in the slurry required to clog the pore network (Gerber et al., 2018). This difference explains why the critical slurry density ρ_{sc} corresponding to the respective percolation threshold was larger for uniformly graded debris than for widely graded debris (Figs. 5E and 5F). ρ_{sc} for uniformly graded debris in our tests is 1275–1297 kg/m³ considering that n is approximately 0.5. However, ρ_{sc} is limited to 1070–1170 kg/m³ for sediment mixtures consisting of sand, gravel and mud due to a small n of ~ 0.32 (Major, 2000). This is probably because the sorting coefficient of the sediment mixtures (2.3–2.4) is larger than that of the uniformly graded debris used in our tests (Table 2). ρ_{sc} is approximately 1195 kg/m³ for $n = 0.36$ –0.38 by comparing the experimental data of Pierson (1981), Kaitna et al. (2016) and de Haas et al. (2015). Therefore, ρ_{sc} can be estimated if n is inferred.

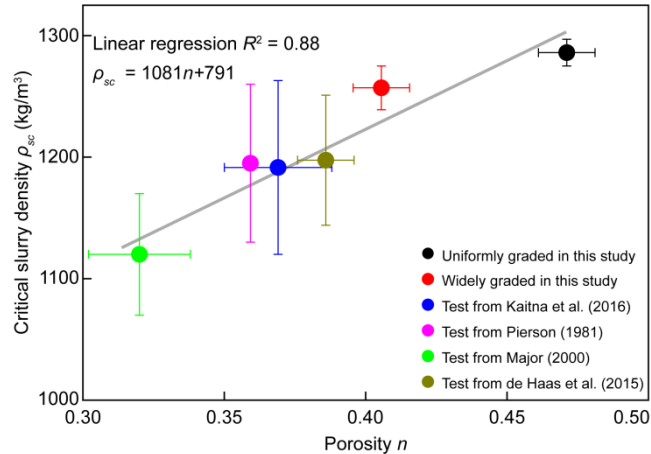


Fig. 8. Critical slurry densities of debris flows versus porosity. Grain-size distributions of debris were within the range of 0.063–32 mm for Major (2000), 0.063–128 mm for Kaitna et al. (2016), and 0.075–5 mm for de Haas et al. (2015). Fines with particle sizes smaller than 63 μm are considered as slurried fines to infer critical slurry density. A large range of slurry density results in a long error bar.

A natural debris flow commonly consists of a coarse-grained front and a flow body with finer-grained debris (Leonardi et al., 2015). One would expect that r_c values in a flow body are smaller than those of the coarse-grained front but ρ_s in the flow body is often higher, leading to lower permeability and diffusion. Field data from natural debris flows show a nonuniform longitudinal distribution of basal pore pressure with low to moderate fluid pressure at the front and a nearly liquefied body (e.g., Berti et al., 2000; McArdell et al., 2007).

5.2 Effect of slurry density on the permeability

The permeability of a debris flow is reduced by pore slurry due to the size exclusion and suspension of kaolin fines (Sharma and Yortsos, 1987). Some fines in the slurry are entrapped in the pore throats, considering the maximum diameter of fines is nearly 45 μm . In addition, clogging of pore throats can occur in the form of fine clusters formed by electrostatic forces (Gerber et al., 2018). The suspension of fines reduces the area allowed for fluid flow. The direct evidence is that the permeabilities of the debris flow in U3–U5 and W3–W4 were low before fines were squeezed out (Fig. 5B).

The hydraulic diffusivity of debris flow in Eq. (1) can be calculated from the dynamic viscosity of the pore slurry, bulk modulus and the permeability of the debris flow measured from constant-head permeameter tests (Iverson et al., 2010). The calculated hydraulic diffusivity matches with the measured values from consolidation tests for debris flows with $\rho_s = 1000 \text{ kg/m}^3$ (pure water), as shown in Fig. 9. However, the calculated hydraulic diffusivity is higher than the measured value and the differences between both values increase with increasing slurry density for uniformly and widely graded mixtures. In particular, we observe a sharp increase in the difference between calculated and measured diffusivity above the critical slurry density. The reason for the deviation between calculated and measured diffusivity is that the permeability reduction of debris flow caused by the pore-throat blockage due to slurry fines is not considered in Eq. (1). In particular, when the critical pore throats are blocked and the connectivity of pore network breaks, the permeability is significantly reduced (Figs. 5E, 5F and 7C).

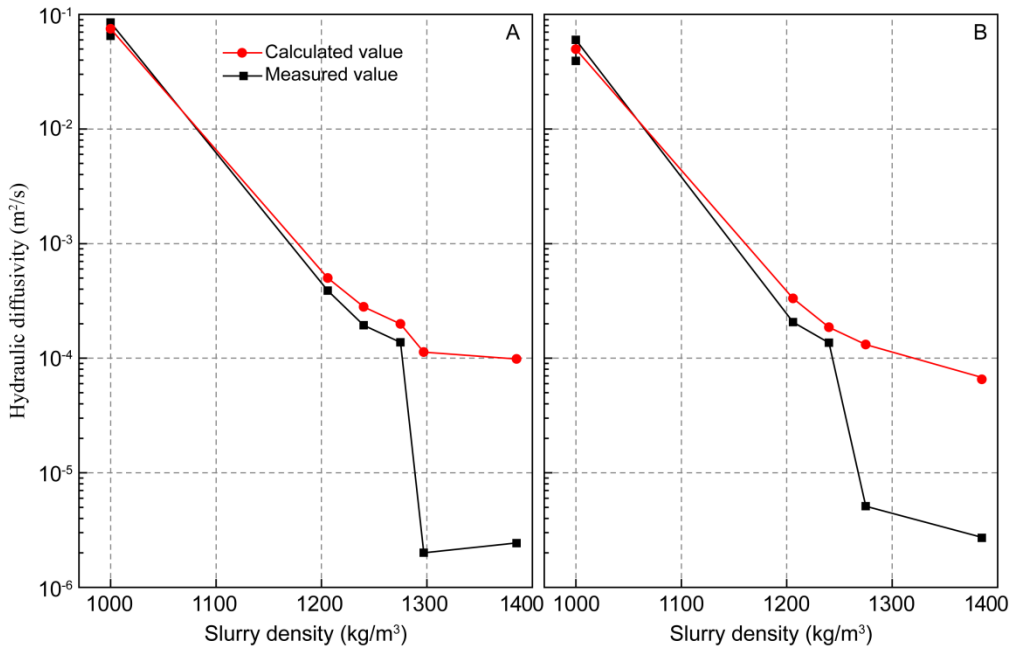


Fig. 9. Measured and calculated hydraulic diffusivities. A: uniformly graded mixtures; B: widely graded mixtures. The differences between the calculated and measured values increase with the increase of slurry density, especially above the critical slurry density.

5.3 Effects of pore pressure on debris-flow behavior

The timescales of propagation and consolidation are of importance for debris-flow behavior (Tayyebi et al., 2021). Debris flows typically have a characteristic propagation time from several minutes to tens of minutes (Iverson et al., 2010). Drained behavior is applicable for debris flows with a low slurry density when propagation time is longer than the consolidation time (several seconds) such as U1–U2 and W1–W2 ($\rho_s = 1000 \text{ kg/m}^3$). Such debris flows cease in a short distance (Fig. 10) because of rapid increases in the effective stress and frictional resistance, displaying sudden freezing in place and swollen deposit lobes (Suwa et al., 2009; Zheng et al., 2021b).

In contrast, debris flows with a high slurry density are likely to display undrained behavior when the propagation time is much smaller than the dissipation time (dozens of hours) such as U6–U7 and W5–W6. In this situation, the increase of effective stress during flow transportation is negligible. Due to a low frictional resistance and a high liquefaction ratio, debris flows can proceed along the entire length of a fan, even on gentle slopes, and deposit as a flat lobe (Hürlimann et al., 2015; Zheng et al., 2021b).

In addition, propagation time can be matched with the time for pore-pressure dissipation like U3–U5 and W3–W4. In this situation, pore pressure of debris flows is maintained during propagation but is dissipated after flows reach the deposition area. Therefore, dissipation timescales of debris flows play a key role in the flow behavior and their dynamics.

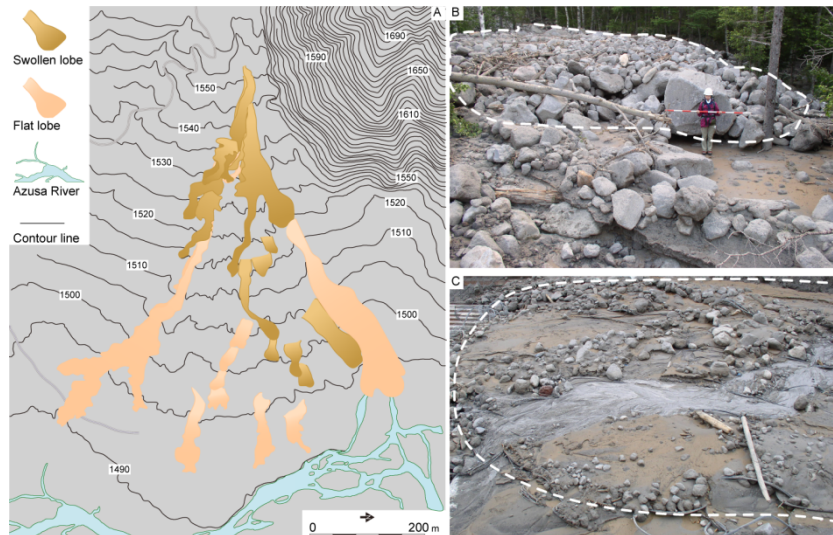


Fig. 10: A: Migration route of debris flows (modified from Suwa et al., 2009). Generally, flows with high slurry density have a longer transport distance than those with low slurry density. B: Swollen deposit lobe of flows with a low slurry density. C: flat deposit lobe of flows with a high slurry density.

5.4 Implications

To the best of our knowledge, the runout distances and planimetric deposition areas of debris flows are commonly predicted by the geomorphologic catchment

parameters (Scheidl and Rickenmann, 2010; Chen et al., 2021). Recently, different machine learning methods, including back-propagation neural network (BPNN), support vector machine (SVM), and extreme learning machine (ELM), have been adopted to predict the flow volume and runout distance (Huang et al., 2020). However, the flow composition, especially slurry density, is not considered among the input parameters for training a neural network. In fact, the excess pore pressure of debris flows has as significant an influence on the flow mobility as the geomorphologic catchment has (McCoy et al., 2010). According to observations in Kamikamihori Gully (Suwa et al., 2009), Susa Valley (Tiranti et al., 2008) and Chalk Cliffs Gully (McCoy et al., 2010), debris flows with a high slurry density possess high pore pressures and travel long distances. In contrast, debris flows with a low slurry density have short runout distances. Furthermore, the critical slurry density has a linear correlation with the porosity of debris flows (Fig. 8). It implies that the existing method for predicting flow mobility can be further modified by considering the slurry density and the consolidation timescale.

The pore throats and their distributions play an important role by setting the permeability of the porous medium. The method we present here can be applied to other types of granular solids with pore spaces filled by interstitial fluid, to explain and quantify conditions that elucidate pore-pressure dissipation and permeability reduction as shown in our tests. For example, rock sample permeability is also significantly affected by the clay fraction (Bourg and Ajo-Franklin, 2017).

5.5 Limitations

The debris samples in consolidation and micro-CT tests were prepared in different processes. The pore networks of debris materials in micro-CT tests were considered to be identical to those in consolidation tests due to the same dry density and grain size distribution. However, the increase in effective stress during consolidation may reduce the sizes of pores and pore throats which would change the permeability of debris material.

The volumetric strain of debris flow ε_v during consolidation is calculated as

$$\varepsilon_v = \varepsilon_z = \frac{\Delta\sigma_e}{E_c} = \frac{p_{e0}}{E_c} \quad (9)$$

where ε_v is equal to uniaxial strain ε_z for one-dimensional consolidation and the increment of effective stress $\Delta\sigma_e$ is equal to the initial excess pore pressure p_{e0} (Table 3). For experimental debris flows presented here, ε_v is smaller than 0.2% for all of the tests due to the limited increase in effective stress. The permeability variation induced by the pore-pressure dissipation may be weak, verifying that micro-CT analysis is appropriate for interpreting consolidation tests here. Caution should be taken for natural debris flows because considerable settlement and permeability change can occur. In those circumstances, on-site sampling is necessary for micro-CT analysis.

6. Conclusions

We quantify the pore networks of debris flow mixtures using micro-CT analysis and find support for the hypothesis that a critical pore throat exists within a debris flow which controls the permeability and hence pore-pressure dissipation. The main concluding remarks are:

(1) Depending on slurry density, pore pressures of debris flow mixtures exhibit three sharply contrasting dissipation modes: fast, slow to fast and slow dissipation. The pore-pressure dissipation times of uniformly and widely graded debris flows increased by approximately two orders of magnitude due to an increase in slurry density of less than 3%.

(2) The pore-throat sizes of debris material are well represented by a truncated Gaussian distribution. The sizes of critical pore throats of uniformly graded and widely graded materials in this study were in the range of 120–150 μm and 90–120 μm , respectively. This difference explains why the critical slurry density corresponding to an abrupt change in dissipation time was larger for uniformly graded debris than for widely graded debris.

(3) The permeability and pore-pressure dissipation of debris flows are regulated by the critical pore throats. When the critical pore throats are clogged, the permeability of a debris flow is significantly reduced, leading to a change in the mode of pore-pressure dissipation and consolidation timescale.

(4) The critical slurry density of a debris flow can be estimated considering that it is approximately linearly correlated with porosity.

Acknowledgments

This research was supported by the National Science Foundation of China (41731283 and 42007252). We thank Jon J. Major for offering their dissipation data of pore pressure. We thank David Mohrig, Bo Li and Hiroshi Suwa for their discussions on the critical pore throat of debris flows. The data in the present work are available online at <https://doi.org/10.5281/zenodo.5716577>.

Notation

a	coefficient for a truncated Gaussian distribution
A	cross section of a surface
C_d	volumetric concentration of debris grains
D	hydraulic diffusivity
E_c	bulk stiffness of the debris material
G	conductance matrix
H	height of deposited debris
k_c	permeability of the debris flow measured from consolidation test
k_m	permeability measured by micro-CT
k_s	permeability of debris material measured from constant-head permeameter test
l	characteristic length of pore throat
n	porosity of debris flow
N_p	pore number
N_c	coordination number
p_e	excess pore pressure of debris flow
p_i	pressure at pore i
q_{ij}	flow rate between pore i and pore j
r	pore-throat radius
r_c	critical pore throat
R^2	determination coefficient
t_d	pore-pressure dissipation time
r_m	mean value of pore throat
u	viscosity of slurry
V_d	debris-grain volume
V_m	debris-flow volume
w	sorting coefficient of debris grain
ρ_s	slurry density
σ^2	variance of pore throat
ρ_{sc}	critical slurry density corresponding to the percolation threshold
ε_v	volumetric strain of debris flow
$\Delta\sigma_e$	increment of effective stress
η	dynamic viscosity
λ_n	eigenvalues

References

- Bardou, E., Ancey, C., Bonnard, C., Vulliet, L., 2003. Classification of debris-flow deposits for hazard assessment in alpine areas, in Rickenmann, D., and Chen, C., eds., *Debris-Flow hazards mitigation: mechanics, prediction, and assessment*, Millpress, Rotterdam, 799–808.
- Berti, M., Genevois, R., LaHusen, R., Simoni, A., Tecca, P.R., 2000. Debris flow monitoring in the Acquabona watershed (Dolomites, Italian Alps). *Phys. Chem. Earth. Part. B.*, 25(9), 707–715.
- Bourg, I.C., Ajo-Franklin, J.B., 2017. Clay, water, and salt: Controls on the permeability of fine-grained sedimentary rocks. *Acc. Chem. Res.* 50, 2067–2074.
- Chen, K.T., Wu, J.H., 2018. Simulating the failure process of the Xinmo landslide using discontinuous deformation analysis. *Eng. Geol.* 239, 269–281.
- Chen, M., Tang, C., Zhang, X., Xiong, J., Chang, M., Shi, Q., Wang, F., Li, M., 2021. Quantitative assessment of physical fragility of buildings to the debris flow on 20 August 2019 in the Cutou gully, Wenchuan, southwestern China. *Eng. Geol.* 293, 106319.
- Cui, R.H., Hassanizadeh S. M., Sun S.Y., 2022. Pore-network modeling of flow in shale nanopores: Network structure, flow principles, and computational algorithms. *Earth-Sci. Rev.* 234, 104203.
- D'Agostino, V., Cesca, M., Marchi, L. 2010. Field and laboratory investigations of runout distances of debris flows in the Dolomites (Eastern Italian Alps). *Geomorphology* 115, 294–304.
- de Haas, T., Braat, L., Leuven, J.R., Lokhorst, I.R., Kleinhans, M.G., 2015. Effects of debris flow composition on runout, depositional mechanisms, and deposit morphology in laboratory experiments. *J. Geophys. Res.-Earth Surf.* 120, 1949–1972.
- de Haas, T., Densmore, A.L., Stoffel, M., Suwa, H., Imaizumi, F., Ballesteros-Cánovas, J.A., Wasklewicz, T., 2018. Avulsions and the spatio-temporal evolution of debris-flow fans. *Earth-Sci. Rev.* 177, 53–75.
- Gerber, G., Rodts, S., Aïmediou, P., Faure, P., Coussot, P., 2018. Particle-size-exclusion clogging regimes in porous media. *Phys. Rev. Lett.* 120(14), 148001.
- Guthrie, R., Hockin, A., Colquhoun, L., Nagy, T., Evans, S., Ayles, C., 2010. An examination of controls on debris flow mobility: evidence from coastal British Columbia. *Geomorphology*, 114, 601–613.
- Hotta, N., and T. Ohta, 2000. Pore-water pressure of debris flows. *Phys. Chem. Earth. Part. B.*, 25(4), 381–386.
- Hu, X.L., Liu, D.Z., Niu, L.F., Liu, C., Wang, X., Fu, R., 2021. Development of soil–pile interactions and failure mechanisms in a pile-reinforced landslide. *Eng. Geol.* 294, 106389.
- Huang, J., Hales, T.C., Huang, R.Q., Ju, N.P., Li, Q., Huang, Y., 2020. A hybrid machine-learning model to estimate potential debris-flow volumes. *Geomorphology*, 367, 107333.
- Hürlimann, M., McArdeell, B.W., Rickli, C., 2015. Field and laboratory analysis of the runout characteristics of hillslope debris flows in Switzerland. *Geomorphology*, 232, 20–32.
- Iverson, R.M. 1997. The physics of debris flows. *Rev. Geophys.* 35, 245–296.
- Iverson, R.M., LaHusen, R.G., 1989. Dynamic pore-pressure fluctuations in rapidly shearing granular materials. *Science*, 246(4931), 796–796.
- Iverson, R.M., Logan, M., LaHusen, R.G., Berti, M. 2010. The perfect debris flow? Aggregated results from 28 large-scale experiments. *J. Geophys. Res.* 115, F03005.
- Iverson, R.M., George, D.L., 2014. A depth-averaged debris-flow model that includes the

- effects of evolving dilatancy: I. Physical basis. *Proc. R. Soc. A* 470, 20130819.
- Jop, P., Forterre, Y., Pouliquen, O., 2006. A constitutive law for dense granular flows. *Nature*, 441(7094), 727–730.
- Kaitna, R., Dietrich, W., Hsu, L., 2014. Surface slopes, velocity profiles and fluid pressure in coarse-grained debris flows saturated with water and mud. *J. Fluid Mech.* 741, 377–403.
- Kaitna, R., Palucis, M.C., Yohannes, B., Hill, K.M., Dietrich, W.E., 2016. Effects of coarse grain size distribution and fine particle content on pore fluid pressure and shear behavior in experimental debris flows. *J. Geophys. Res.-Earth Surf.* 121, 415–441.
- Kirkpatrick, S. 1973. Percolation and Conduction. *Rev. Mod. Phys.* 45, 574–588.
- Leonardi, A., Cabrera, M., Wittel, F.K., Kaitna, R., Mendoza, M., Wu, W., Herrmann, H.J., 2015. Granular front formation in free-surface flow of concentrated suspensions. *Physical Review E*, 92, 052204.
- Major, J.J., 2000. Gravity-driven consolidation of granular slurries: implications for debris-flow deposition and deposit characteristics. *Journal of Sedimentary Research*, 70, 64–83.
- McArdell, B.W., Bartelt, P., Kowalski, J., 2007. Field observations of basal forces and fluid pressure in a debris flow. *Geophys. Res. Lett.* 34(7), L07406.
- McCoy, S.W., Kean, J.W., Coe, J.A., Staley, D.M., Wasklewicz, T.A., Tucker, G.E., 2010. Evolution of a natural debris flow: in situ measurements of flow dynamics, video imagery, and terrestrial laser scanning. *Geology*, 38, 735–738.
- Nagl, G., Huebl, J., Kaitna, R., 2020. Velocity profiles and basal stresses in natural debris flows. *Earth Surf. Process. Landf.* 45(8), 1764–1776.
- Pierson, T.C., 1981. Dominant particle support mechanisms in debris flows at Mt Thomas, New Zealand and implications for flow mobility. *Sedimentology*, 28(1), 49–60.
- Pudasaini, S.P., 2012. A general two-phase debris flow model. *J. Geophys. Res.-Earth Surf.* 117, F03010.
- Scheidl, C., Rickenmann, D., 2010. Empirical prediction of debris-flow mobility and deposition on fans. *Earth Surf. Process. Landf.* 35, 157–173.
- Sharma, M.M., Yortsos, Y.C., 1987. Fines migration in porous media. *AIChE Journal*, 33, 1654–1662.
- Suwa, H., Okano, K., Kanno, T., 2009. Behavior of debris flows monitored on test slopes of Kamikamihorizawa Creek, Mount Yakedake, Japan. *International Journal of Erosion Control Engineering*, 2, 33–45.
- Takahashi, T., 2007. *Debris flow: mechanics, prediction and countermeasures*. Taylor and Francis, London.
- Taylor, H.F., O’Sullivan, C., Sim, W.W., 2015. A new method to identify void constrictions in micro-CT images of sand. *Comput. Geotech.* 69, 279–290.
- Tayyebi, S.M., Pastor, M., Stickle, M.M., 2021. Two-phase SPH numerical study of pore-water pressure effect on debris flows mobility: Yu Tung debris flow. *Comput. Geotech.* 132(2):103973.
- Terzaghi, K., 1943. *Theoretical soil mechanics*. John Wiley.
- Tiranti, D., Bonetto, S., Mandrone, G., 2008. Quantitative basin characterisation to refine debris-flow triggering criteria and processes: an example from the Italian Western Alps. *Landslides*, 5, 45–57.
- Wang, G., Sassa, K., Fukuoka, H., 2003. Downslope volume enlargement of a debris slide–debris flow in the 1999 Hiroshima, Japan, rainstorm. *Eng. Geol.* 69, 309–330.
- Zheng, H., Shi, Z., Peng, M., Yu, S., 2018. Coupled CFD-DEM model for the direct numerical simulation of sediment bed erosion by viscous shear flow. *Eng. Geol.* 245, 309–321.

- Zheng, H., Shi, Z., Yu, S., Fan, X., Hanley, K. J., Feng, S., 2021a. Erosion mechanisms of debris flow on the sediment bed. *Water Resour. Res.* WR030707.
- Zheng, H., Shi, Z., Hanley, K. J., Peng, M., Guan, S., Feng, S., Chen, K., 2021b. Deposition characteristics of debris flows in a lateral flume considering upstream entrainment. *Geomorphology*, 107960.
- Zheng, H., Shi, Z., de Haas, T., Shen, D., Hanley, K. J., Li, B., 2022. Characteristics of the impact pressure of debris flows. *J. Geophys. Res.-Earth Surf.* 127, 2021JF006488.